

Mechanical Response of the Endothelial Glycocalyx to Pulsatile Flow

Author: Arnau Perdigó Oliveras

Supervisor: Dr Peter E Vincent



*Department of Aeronautics, Imperial College London,
South Kensington Campus, London SW7 2AZ*

July 2012

To my parents, Josep Ma. Perdigó and Ma. Dolors Oliveras, without whose effort and continuous support I would not have had the opportunity to research at Imperial College London.

Acknowledgements

First of all, I would like to thank everyone who has contributed to this project:

- Dr Peter E Vincent, my supervisor, has guided me through the research process of this project, having always the cleverest piece of advice at every progress review meeting we had. His guidance could not have been better.
- Veronique Peiffer provided me with exquisitely presented essential data and explained me a few tricks to deal with it.
- Dr Peter Weinberg motivated me even further to develop the mechanical model of the glycocalyx when he explained to me how the patterns of atherogenesis evolve with age.
- Ravi Khiroya is working on a different method to solve the presented model in order to double-check my results and maybe increase precision and speed up calculations.
- Mark Van Logtestijn and Luca Pesaresi helped me find a few bugs and inspired some solutions for my MATLAB code.

Your collaboration, guidance, help, inspiration and support has been invaluable. Thank you very much.

Abstract

The endothelial glycocalyx is a thin layer lining the internal wall of all blood vessels. It is in the arteries wall where cholesterol and other fatty materials can accumulate eventually obstructing the blood flow and causing atherosclerosis and other vascular diseases to occur. Although the correlation between regions of this arterial disease and areas with low and disturbed wall shear stress has been established, its patterns still do not match.

The glycocalyx is considered to be responsible for the transduction of the fluid-induced shear stress to biomechanical forces in the endothelium. A mechanical model of the glycocalyx as a dense matt of regularly distributed stiff rods attached to the endothelial cell membrane and subject to the wall shear stress and drag forces has been developed to study how blood flow forces are actually 'felt' by the arterial wall.

It is found that for oscillating forces with high amplitude, compared to its average value, the frequency of the applied force is a key factor to determine the actual pulling force transferred through the fibres of the glycocalyx to the endothelium. However, the post-processing of simulated wall shear stress in a rabbit's descending thoracic aorta with the developed mechanical model has not revealed major changes in the transduced force pattern.

Contents

Acknowledgements.....	1
Abstract.....	3
1 Introduction.....	7
1.1 The endothelial glycocalyx.....	7
1.2 Atherosclerosis.....	7
1.3 Motivation and intention of this project.....	8
2 The one dimensional model.....	9
2.1 Model discussion.....	9
2.2 Governing equation.....	12
2.3 Model parameter values.....	14
2.4 Simplification of the governing equation.....	14
2.5 Non-dimensionalisation.....	15
2.6 Numerical solution.....	15
2.7 Post-processing.....	16
3 1D model results.....	19
3.1 With fixed average force.....	19
3.2 With fixed force amplitude.....	20
4 The two dimensional model.....	21
4.1 Model discussion and system of governing equations.....	21
4.2 Numerical solution and post-processing.....	23
5 Study of simulated shear stress in a rabbit's blood vessel.....	25
5.1 Original data and previous considerations.....	25
5.2 Analysis of specific data points.....	27
5.3 2D model results in the 3D geometry.....	28
6 Conclusions and future research.....	33
6.1 Conclusions.....	33
6.2 Future research.....	33
Nomenclature.....	35
Bibliography.....	37

1 Introduction

1.1 The endothelial glycocalyx

The endothelial glycocalyx layer (glycocalyx), also known as the endothelial surface layer, is a bushy, gel-like layer of 200-500nm of thickness (Nieuwdrop et al. [1]) that covers the inner wall of all blood vessels, i.e. a total area of 350m² in an average human (Pries et al. [2]). According to Reitsma et al. [3], the glycocalyx is mainly formed by proteoglycans (consisting of a core protein linking glycosaminoglycans) and glycoproteins, also incorporating plasma and other soluble molecules.

Van der Berg et al. [4] obtained in 2003 an electron microscopic, cross-section view of a rat's left ventricular myocardial (see Figure 1-1) in which the 'hairy' glycocalyx layer can be observed extending from the arterial wall towards the lumen.

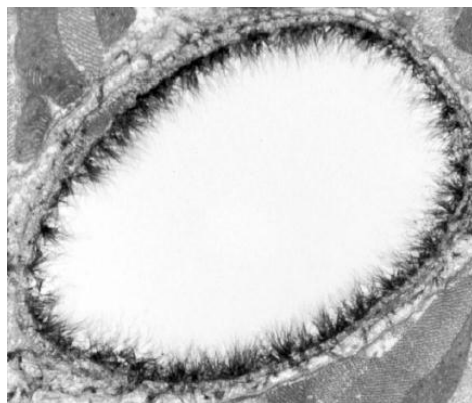


Figure 1-1 Cross-section view of a rat's ventricular myocardial (source: van der Berg et al. [4])

Given the location of the glycocalyx layer, between the blood flow and the endothelial cell membrane, its main function is the regulation of vascular fluid exchange across the endothelial wall (Reitsma et al. [3]). It also plays a role in the oxygen transport from red cells to tissue, while preventing the firsts from interacting directly with the endothelium. The glycocalyx is also known to act as a mechanotransducer of the blood stream's induced shear stress to biomechanical forces on endothelial cells (Weinbaum et al. [5]). According to the report by Weinbaum et.al [6] and Reitsma et al. [3], the glycocalyx shear stress transduction results in endothelial cell morphology and function adjustments.

1.2 Atherosclerosis

Atherogenesis is the process by which fatty materials, such as cholesterol, accumulate in the artery walls, thickening and hardening them and eventually leading to the vessel's obstruction. This vascular disease, known as atherosclerosis, leads today's death cause in developed countries.

The phenomenon of atherogenesis occurs non-uniformly across the endothelial cell surface. It has been established that regions with low and oscillating wall shear stress seem to favour the development of atherosclerosis (Shabaan et al. [7]). However, as seen in Vincent et al.'s article "Blood flow in the rabbit aorta" [8], atherosclerosis' early stage patterns, although resemble, do not match those of wall shear stress (see Figure 1-2 and Figure 1-3).

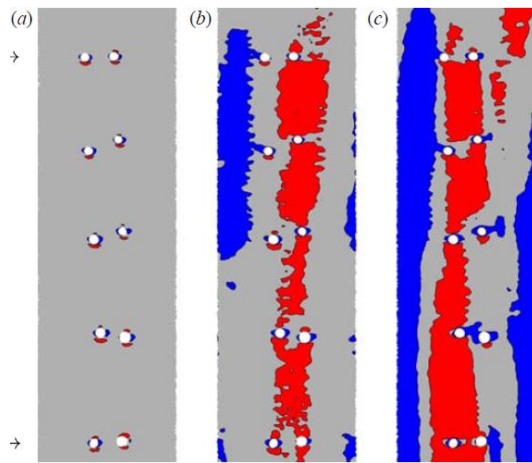


Figure 1-2 Wall shear stress pattern (red: high, grey: average, blue: low) in the rabbit's descending aorta for three values of flow's Reynolds number (increasing left to right) (source: Vincent et al. [8])

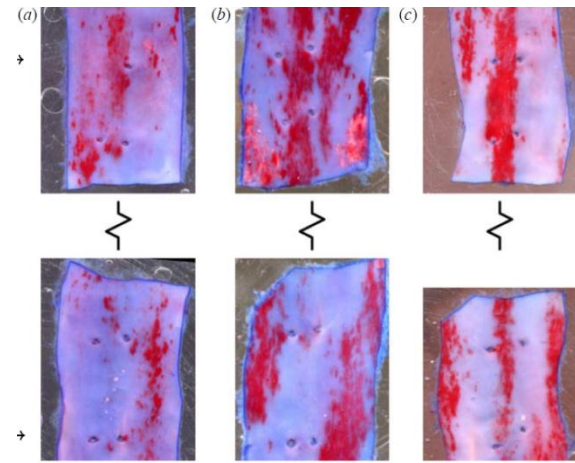


Figure 1-3 Fatty deposits identified in red from 3 different rabbit's descending aorta (source: Vincent et al. [8])

This is one of the reasons why the glycocalyx has been increasingly considered to play an important role in vascular pathologies, the most important of those being atherosclerosis.

1.3 Motivation and intention of this project

Pries et al. [2] stated in their report "The endothelial surface layer" that «*More work is needed to understand the role of the endothelial surface layer in the response of endothelial cells to shear stress*», whilst the British Heart Foundation (BHF) states its vision to be «*A world where people no longer die prematurely from heart disease*» and consequently sets its commitment to research, information and campaigning, amongst others.

It is in this context of scientific claim for further research on the mechanical response of the glycocalyx, and also humans' need to address a leading cause of death that this project aims to develop a mechanical model of the glycocalyx to study its dynamic response to the pulsatile blood flow.

2 The one dimensional model

In this chapter, the first approach to model mechanically the glycocalyx is discussed and mathematically expressed. Furthermore, the solving process and final metric calculation are also discussed.

To start with, a simplistic one dimensional (1D) model was developed in order to assess the importance of the shear stress being pulsatile to the glycocalyx' induced dynamics.

2.1 Model discussion

For the reasons mentioned in 1 Introduction, the properties of the glycocalyx have been extensively researched over the past decade. Yet, there is still some uncertainty on how its structure actually is (Reitsma et al. [3]) and, specifically, how it behaves mechanically when exposed to the pulsatile blood flow. That is why a very simplistic model was required: no unknown or uncertain properties had to be implied by the developed mechanical model.

The hypothetical structure of the glycocalyx shown in Figure 2-1, proposed by Pries et al. [2], who also state that «*shear stress must be mainly transmitted to the endothelial surface via the glycocalyx*», suggested that the shear stress caused by the dynamic equilibrium between the flowing blood and the glycocalyx layer is transferred to the endothelial cell membrane in two stages: through the thick, insides gel-like layer (adsorbed plasma proteins and glycosaminoglycans) and through the cell attached glycocalyx (formed by core protein fibres attached to the endothelial cells).

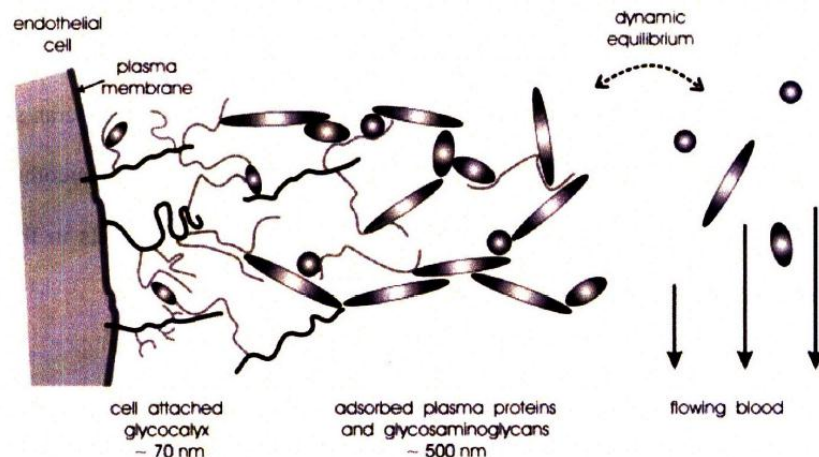


Figure 2-1 Hypothetical composition of the Glycocalyx (source: Pries et al. [2])

A similar model for the glycocalyx' structure to the one shown in Figure 2-1 had also been proposed by Reitsma et al. [3] and Weinbaum et al. [6].

Interestingly, previous research work by Yao [9] showed the cell-attached glycocalyx' core protein fibres bend down and recoil, as had previously been predicted by Han et al. [10] (see Figure 2-2). Intuitively, pulsatile shear stress acting on fibres of such flexural characteristics would lead to time-frequency dynamics of the fibres.

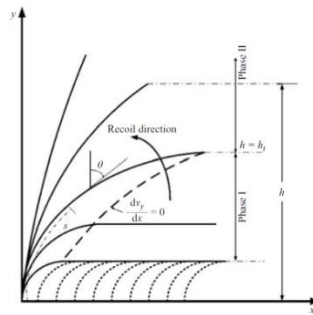


Figure 2-2 Large-deformation recovery of core protein fibres (source: Han et al. [10])

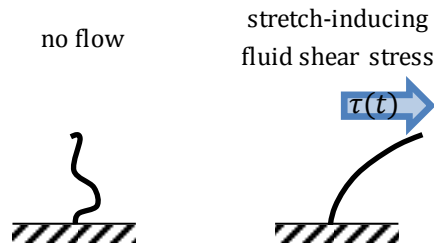


Figure 2-3 Fibre stretching due to fluid shear stress

In the mentioned studies, [9] and [10], it is suggested that the cell-attached chains, which might not be straight without the presence of fluid shear stress, do actually extend when blood flows on top of them (see Figure 2-3). This had also been hypothesised by Pries et al. [2], in whose paper the simplistic model in Figure 2-4 for the chains forming the glycocalyx to transmit tension is presented, and in the mechano-electrochemical models described in Weinbaum et al.'s report [5], which assume the glycocalyx to be in a «state of axial tension».

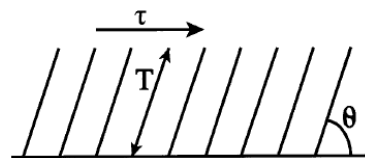


Figure 2-4 Diagram of fibres supporting shear stress and consequently transmitting tension (source: Pries et al. [2])

Similarly, the mechanical model of the glycocalyx showed in Figure 2-5 was proposed. The differentiation of the two regions of the glycocalyx was the following one: the inner gel-like layer was supposed to transmit the shear stress from the surface in dynamic equilibrium with the blood flow to the one in equilibrium with the cell-attached glycocalyx. This second region was modelled as uniformly distributed straight rods attached to the endothelium. The mentioned rods would be able to transmit the force applied on top of it. The resulting pulling force on the endothelium would therefore depend on the angle rotated by such rod.

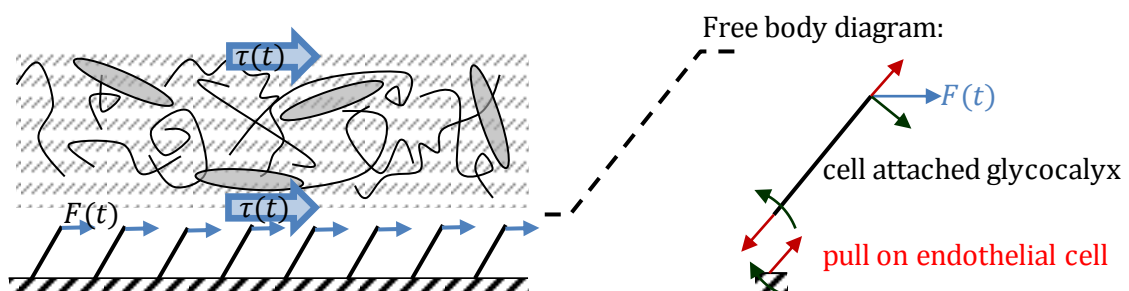


Figure 2-5 Shear stress transmission through the glycocalyx

To model the flexural rigidity, the rod would be articulated on its base with a rotational spring. That would allow it to rotate down under the action of a force and recoil afterwards. Rotational friction would account for the drag of the moving fibre through the plasma. Geometrically, this rod would be cylindrical and have its mass uniformly distributed along its length.

The resulting model with the articulated rod, the applied forces, i.e. rotational spring torque ($K \cdot \theta$), drag force (F_D) and driving force ($F(t)$), its parameters (m, L) and coordinate system used ($\theta(t), r$) is schematically shown in [Figure 2-6](#). A more in-depth presentation of all these parameters is made in [2.2 Governing equation](#).

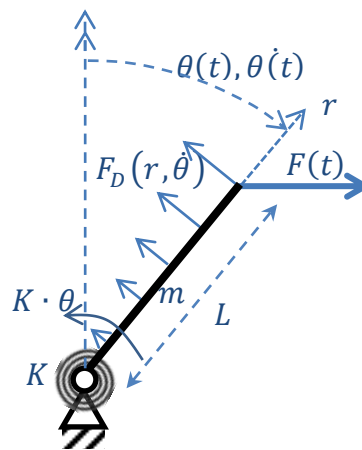


Figure 2-6 Single glycoalyx' fibre diagram

However, to restrict the extension of this project, the following simplifications were made:

- The rod was always considered to be straight. It was not that the actual bending of the fibre was being neglected, but that it was instead modelled with the entire straight rod turning down.
- The interaction between adjacent rods was not considered in any other way than: (1) the Darcy permeability of the glycoalyx, used in [2.2 Governing equation](#) to calculate the drag force that a turning rod experiences, takes into account the distribution and density of rods in the surface. And (2) the patterns of shear stress τ (and therefore, those of the driving forces) already vary smoothly across the endothelium. That means that adjacent rods would have similar dynamics as a consequence of having similar driving forces.
- Gravity forces were not considered.
- The rotational spring, responsible for modelling the stiffness of the rod, was considered to load linearly with the rotated angle, despite the results found by Yao [9] indicating that the shear modulus of the glycoalyx layer (G) could vary up to $\pm 25\%$ depending on the applied shear stress τ . To this dissertation's author's understanding, though, the variation of the shear modulus could be actually related to the layer's deformation as a consequence of the applied τ . Because the model discussed in this dissertation does only consider the cell-attached glycoalyx' deformation, the variation of G could be imprecisely calculated. Moreover, the aim was to keep the model "nice and simple".

2.2 Governing equation

The differential equation governing the aforementioned model is the following one:

$$I \cdot \ddot{\theta}(t) + C \cdot \dot{\theta}(t) + K \cdot \theta(t) = F(t) \cdot L \cdot \cos(\theta(t)) \quad (\text{Eq 2-1})$$

Where:

- $\theta(t)$ is the angle rotated by the rod [rad].
- I is the inertia of the rod [$kg \cdot m^2$], which depends on its mass (m [kg]) and length (L [m]). The corresponding cylinder inertia is:

$$I = \frac{m \cdot L^2}{3} \quad (\text{Eq 2-2})$$

- C is the coefficient of rotational friction [$\frac{N \cdot m}{s \cdot rad}$], modelling the drag force experienced by the turning rod in the plasma-like media. According to Weinbaum et al. [5], such drag force F_D [N] can be calculated as follows:

$$F_D(r, \dot{\theta}) = \frac{\pi \cdot \mu \cdot \dot{\theta} \cdot r}{3 \cdot v_f} \cdot \frac{r_f^2}{K_p} \quad (\text{Eq 2-3})$$

Here μ is the plasma viscosity [$Pa \cdot s$], r_f is the fibre radius [m], v_f is the fibre volume fraction [unitless], K_p is the Darcy permeability of the glycocalyx [m^2] and Δ is the fibre gap [m]. Parameters v_f and K_p can be calculated using (Eq 2-4) and (Eq 2-5) formulas. While the former obeys to an idealised geometrical distribution of the hairs in the cell-attached glycocalyx proposed by Weinbaum et al. [5] (see Figure 2-7), the latter is based on results found by Sadiq et al. [11] and Sangani et al. [12] and is valid for $v_f < 0.4$.

$$v_f = \frac{2 \cdot \pi \cdot r_f^2}{\sqrt{3} \cdot (2 \cdot r_f + \Delta)^2} \quad (\text{Eq 2-4})$$

$$K_p = r_f^2 \cdot \frac{\ln\left(\frac{1}{\sqrt{v_f}}\right) - 0.745 + v_f - \frac{v_f^2}{4}}{4 \cdot v_f} \quad (\text{Eq 2-5})$$

Finally, the coefficient C can be calculated integrating the drag force along the length of the rod as shown in (Eq 2-6):

$$C = \frac{1}{\dot{\theta}(t)} \cdot \int_0^L F_D(r, \dot{\theta}(t)) \cdot r \cdot dr = \frac{L^3 \cdot \pi \cdot \mu \cdot r_f^2}{3 \cdot v_f \cdot K_p} \quad (\text{Eq 2-6})$$

- K is the coefficient of a torsion spring [$\frac{N \cdot m}{rad}$] which models the stiffness of the rod. It has been deduced from the definition of the shear modulus (G [Pa]) (Eq 2-7):

$$G = \frac{\tau}{\tan(\theta)} = \frac{F \cdot N}{\tan(\theta)} \quad (\text{Eq 2-7})$$

The shear stress (τ [Pa]) is equal to the number of rods per area unit (N [$\frac{1}{m^2}$]) times the force applied to each rod (F [N]). N is calculated for the hexagonal distribution of rods attached to the endothelium (see Figure 2-7) proposed by Weinbaum et al. [5] and calculated in (Eq 2-8).

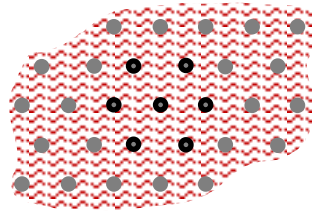


Figure 2-7 Idealised geometrical distribution of rods on the endothelium

$$N = \frac{2}{\sqrt{3} \cdot (2 \cdot r_f + \Delta)^2} \quad (\text{Eq 2-8})$$

Linearizing (Eq 2-7) for $\theta \rightarrow 0$ with: $\tan(\theta) \approx \theta \approx \frac{L \cdot F}{K}$, the formula in (Eq 2-9) for the coefficient K is obtained:

$$K \approx \frac{L \cdot G}{N} \quad (\text{Eq 2-9})$$

- $F(t)$ is the driving force applied on top of each rod [N]. For the purposes of testing this model and assessing for the first time the importance of the frequency response of the glycocalyx to a pulsatile perturbation, this force was temporarily assumed to have the idealised form described by (Eq 2-10) and shown in Figure 2-8.

$$F(t) = A \cdot \cos(\omega \cdot t) + F_0 \quad (\text{Eq 2-10})$$

Here A is the amplitude of the force [N], $\omega = 2\pi \cdot f$ represents its angular frequency [Hz] and F_0 is the offset around which the force oscillates [N].

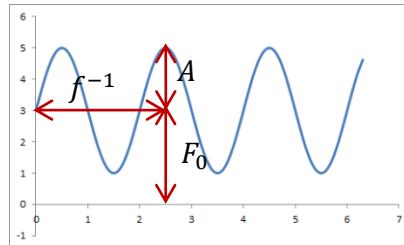


Figure 2-8 Idealised driving force's parameters

2.3 Model parameter values

The parameters that appear in the governing equation depend on the characteristics of the glycocalyx. Table 2-1 shows these characterising parameters and the references that were used to determine them.

Description	Parameter value	Comments
Rod's mass	$m = 1.66 \cdot 10^{-20} \text{ kg}$	According to Reitsma et al. [3], high-weight glycosaminoglycan chains present in the glycocalyx have a mass of up to 10^4 kDa.
Rod's length	$L = 70 \cdot 10^{-9} \text{ m}$	Pries et al. [2] stated the thickness of the glycocalyx to be comprised between 70nm and 400nm, being the lowest value the one associated with the cell-attached glycocalyx.
Plasma viscosity	$\mu = 1.6 \cdot 10^{-3} \text{ Pa} \cdot \text{s}$	Value of the blood plasma viscosity measured by Haidekker et al. [13] using fluorescent molecular rotors.
Fibre gap	$\Delta = 8 \cdot 10^{-9} \text{ m}$	From the structural model of the glycocalyx presented in Weinbaum et al. [5], consistent with results from Curry et al. [14] (center-to-center spacing around 20 nm)
Fibre radius	$r_f = 6 \cdot 10^{-9} \text{ m}$	
Shear modulus	$G = 6.7 \text{ Pa}$	Yao [9], calculated it using an imaging technique tracing the motion of quantum dots attached to the glycocalyx and stated that $G = 6.7 \pm 3.3 \text{ Pa}$.

Table 2-1 Defining parameters: glycocalyx characteristics

As a result, dependant parameters shown in Table 2-2, and particularly I , C and K (highlighted in blue) which appear in the governing equation, could be calculated:

Description	Parameter value	Comments
Rod's inertia	$I = 5.54 \cdot 10^{-35} \text{ kg} \cdot \text{m}^2$	
Fibre volume fraction	$v_f = 0.326$	Validates the equation (Eq 2-5) for the Darcy permeability of the glycocalyx ($v_f < 0.4$).
Darcy permeability of the glycocalyx	$K_p = 3.37 \cdot 10^{-19} \text{ m}^2$	In some references, and particularly in the article by Sadiq et al. [11], it is also expressed as the non-dimensional parameter $\frac{K_p}{r_f^2} = 9.35 \cdot 10^{-3}$ [unitless].
Rotational friction coefficient	$C = 1.88 \cdot 10^{-22} \frac{\text{N} \cdot \text{m}}{\text{s} \cdot \text{rad}}$	
Number of rods per area unit	$N = 2.89 \cdot 10^{15} \frac{1}{\text{m}^2}$	
Rotational spring coefficient	$K = 1.62 \cdot 10^{-22} \frac{\text{N} \cdot \text{m}}{\text{rad}}$	

Table 2-2 Calculated parameters, including I , C and K

2.4 Simplification of the governing equation

From the results in Table 2-2 it turned out that: $I \sim 10^{-13} \cdot C$, $I \sim 10^{-13} \cdot K$. Therefore, the governing equation could be simplified by omitting I to the first-order, nonlinear differential equation shown in (Eq 2-11):

$$C \cdot \dot{\theta}(t) + K \cdot \theta(t) = F(t) \cdot L \cdot \cos(\theta(t)) \quad (\text{Eq 2-11})$$

2.5 Non-dimensionalisation

Given the high dependence of the governing equation's parameters on the characteristics of the glycocalyx, it was a good practice to non-dimensionalise it in a convenient manner. Using (Eq 2-10) in (Eq 2-11) and dividing the resulting equation by K one obtains (Eq 2-12):

$$\frac{C}{K} \cdot \dot{\theta}(t) + \theta(t) = \frac{A \cdot L}{K} \cdot (\cos(\omega \cdot t) + F_0) \cdot \cos(\theta(t)) \quad (\text{Eq 2-12})$$

The new non-dimensional parameters were defined in (Eq 2-13) to (Eq 2-15):

$$\hat{t} = \frac{t \cdot C}{K}, \quad \frac{d}{dt} = \frac{K}{C} \cdot \frac{d}{d\hat{t}} \quad [\text{unitless}] \quad (\text{Eq 2-13})$$

$$\hat{\omega} = \frac{\omega \cdot K}{C} \quad [\text{unitless}] \quad (\text{Eq 2-14})$$

$$\hat{A} = \frac{A \cdot L}{K}, \quad \hat{F}_0 = \frac{F_0 \cdot L}{K} \quad [\text{unitless}] \quad (\text{Eq 2-15})$$

Consequently, the governing equation could be expressed in terms of these new parameters and variable as follows:

$$\dot{\theta}(\hat{t}) + \theta(\hat{t}) = (\hat{A} \cdot \cos(\hat{\omega} \cdot \hat{t}) + \hat{F}_0) \cdot \cos(\theta(\hat{t})) \quad (\text{Eq 2-16})$$

A solution of this equation would therefore be valid for the chosen values of \hat{A} , \hat{F}_0 and $\hat{\omega}$, which can correspond to different combinations of the actual characteristics of the glycocalyx (length, spacing, stiffness...). Hence, the convenience of this non-dimensionalisation.

2.6 Numerical solution

Given the absence of analytical solutions for the governing equation (Eq 2-16) caused by its specific non-linearity, it was mandatory to use numerical methods to reach an accurately enough numerical solution. It was chosen to solve it as an initial value problem (IVP), using the static equilibrium angle (β [rad]) (see Figure 2-9) calculated in (Eq 2-17) as initial condition: $\theta(\hat{t} = 0) = \beta$.

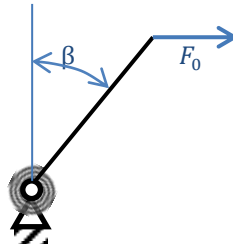


Figure 2-9 Static equilibrium angle β

$$F_0 \cdot L \cdot \cos(\beta) = K \cdot \beta; \quad \hat{F}_0 \cdot \cos(\beta) = \beta \implies \beta \quad (\text{Eq 2-17})$$

The solving algorithm employed MATLAB's built-in *ode45* solver, which uses a fourth-order Runge-Kutta method with variable step size. The solution for $\theta(\hat{t})$ was then calculated with the mentioned algorithm until it reached a steady state with a certain precision.

In order to double-check the accuracy of the algorithm when solving such non-linear differential equation, a further verification was performed using the *Manufactured Solutions Method*: Given (Eq 2-16) and an arbitrarily manufactured solution $Y(\hat{t})$, the residual $\Gamma(\hat{t})$ can be calculated as in (Eq 2-18). Then solving (Eq 2-19) with the algorithm being checked must lead to $\theta(\hat{t}) = Y(\hat{t})$.

$$\dot{Y}(\hat{t}) + Y(\hat{t}) - (\hat{A} \cdot \cos(\hat{\omega} \cdot \hat{t}) + \hat{F}_0) \cdot \cos(\theta(\hat{t})) = \Gamma(\hat{t}) \quad (\text{Eq 2-18})$$

$$\dot{\theta}(\hat{t}) + \theta(\hat{t}) = (\hat{A} \cdot \cos(\hat{\omega} \cdot \hat{t}) + \hat{F}_0) \cdot \cos(\theta(\hat{t})) + \Gamma(\hat{t}) \quad (\text{Eq 2-19})$$

In regards to the values of the non-dimensional parameters appearing in the equation to be solved, (Eq 2-16), a range of them was chosen for each parameter in order to generate a map of solutions (see 3 1D model results). Table 2-3 specifies these parameters' ranges:

Parameters' values	Comments
$\widehat{\omega} \in 0 - 9$	It corresponds approximately to $f \in 0 - 1.25$ Hz, which according to [15] is a sensible range.
$\widehat{A} \in 0 - 3$	Corresponding to $\tau \in 0 - 20$ Pa, the range of shear stress values found in simulations by [16].
$\widehat{F}_0 \in 0 - 3$	

Table 2-3 Ranges for the non-dimensional parameters

2.7 Post-processing

Once each solution of $\theta(\hat{t})$ for a certain combination of values of the non-dimensional parameters had been found, a further calculation was performed in order to determine the actual pull being transferred to the endothelial cell membrane. This calculation consisted in taking the driving force in the direction of the rod $\widehat{F}_p(\hat{t})$ (Eq 2-20) and integrating it through all the intervals within one period of the steady state for which the rod was under traction (Eq 2-21).

$$\widehat{F}_p(\hat{t}) = \widehat{F}(\hat{t}) \cdot \sin(\theta(\hat{t})) = (\widehat{A} \cdot \cos(\widehat{\omega} \cdot \hat{t}) + \widehat{F}_0) \cdot \sin(\theta(\hat{t})) \quad (\text{Eq 2-20})$$

$$\overline{\text{Pull}} = \sum_{n=0}^{n_m} \int_{\hat{t}=\widehat{t}_s+\widehat{t}_{2n}}^{\hat{t}=\min\{\widehat{t}_s+\widehat{t}_{2n+1}, \widehat{t}_s+\widehat{T}\}} \widehat{F}_p(\hat{t}) \cdot d\hat{t} \quad (\text{Eq 2-21})$$

In (Eq 2-21), n is an ascending integer number (0, 1, 2...), n_m is the value of n for which $\widehat{t}_s + \widehat{t}_{2(n_m+1)} > \widehat{T}$, \widehat{t}_s is an arbitrary value of \hat{t} for which $\theta(\hat{t})$ has reached the steady state, $\widehat{T} = \frac{1}{2\pi \cdot \widehat{\omega}}$ is the non-dimensional oscillation period of both the driving force and the rod's turned angle, and $[\widehat{t}_s + \widehat{t}_{2n} \quad \widehat{t}_s + \widehat{t}_{2n+1}]$ is an interval of \hat{t} for which $\widehat{F}(\hat{t}) \cdot \theta(\hat{t}) > 0$. This last condition stands for the rod being under traction, as diagrams in Figure 2-10 show:

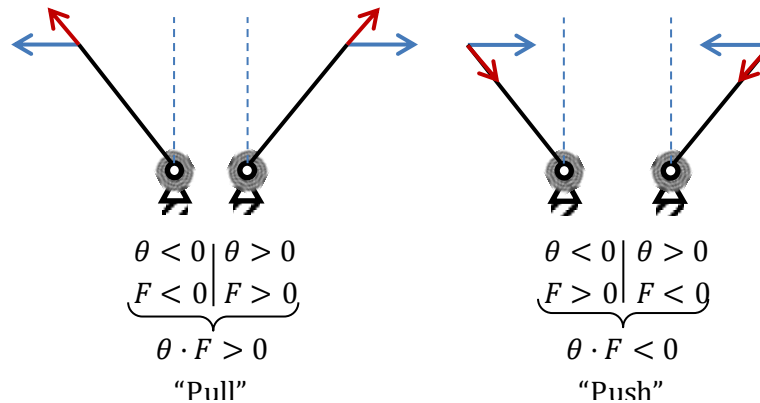


Figure 2-10 Diagrams of the rod being under traction and compression respectively

The consideration that compressive forces cannot be transmitted through the cell-attached glycocalyx is consistent with the conclusions from Weinbaum et al.'s report [6], in which it is predicted that the flexural rigidity of the core proteins is inadequate to prevent its buckling when subjected to compressive forces.

In the example represented in Figure 2-11, the intervals in which the rod is tractioned are: $\hat{t}_s + \hat{t}_0 - \hat{t}_s + \hat{t}_1$ and $\hat{t}_s + \hat{t}_2 - \hat{t}_s + \hat{t}_3$. Note that in these intervals θ and \hat{F} do have the same sign and therefore $\hat{F}_p(\hat{t}) \cdot \sin(\theta(\hat{t}))$ can be integrated as the pull transmitted through the rod as shown in (Eq 2-22).

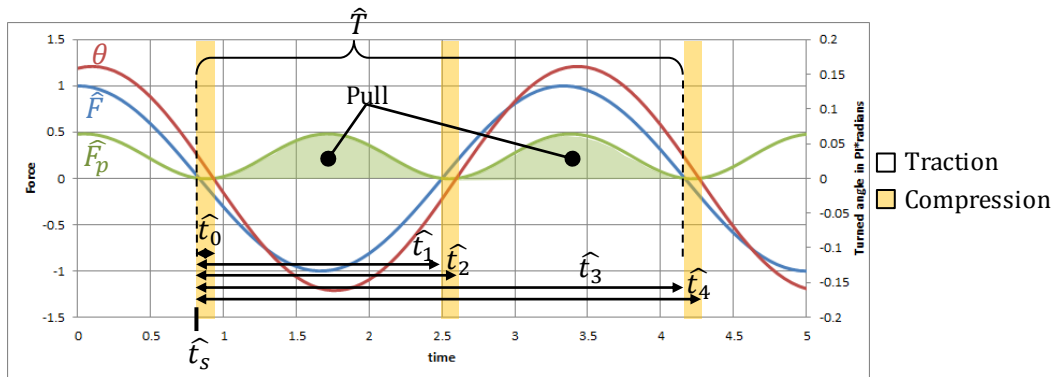


Figure 2-11 Example of post-process calculation of Pull

$$\widehat{Pull} = \int_{\hat{t}=\hat{t}_s+\hat{t}_0}^{\hat{t}=\hat{t}_s+\hat{t}_1} \hat{F}_p(\hat{t}) \cdot d\hat{t} + \int_{\hat{t}=\hat{t}_s+\hat{t}_2}^{\hat{t}=\hat{t}_s+\hat{t}_3} \hat{F}_p(\hat{t}) \cdot d\hat{t} \quad (\text{Eq 2-22})$$

Finally, the result was averaged over the period (Eq 2-23) to make it comparable between cases with different angular frequencies of the shear stress oscillation.

$$\widehat{pull} = \frac{\widehat{Pull}}{\hat{T}} \quad (\text{Eq 2-23})$$

It is worth noticing that \widehat{pull} is, by definition, positive and smaller than the value of the average shear stress over the period. Yet, it was not the specific value of each numeric what was being considered. Instead, the interest was in finding out whether the pattern of each numeric on the endothelial cell surface did match the one of the atherogenesis.

3 1D model results

Results obtained from solving the rod's steady state dynamic response to different pulsatile driving forces (for different values of \hat{A} , \hat{F}_0 and $\hat{\omega}$) were used to calculate the transferred force ($\hat{p}ull$) in each case. Such results were vast and thus, laborious to analyse at a first glance. In this chapter, they are presented and analysed in different "slices". All 1D results were calculated using the non-dimensionalising parameter values from [2.3 Model parameter values](#).

3.1 With fixed average force

For the particular case of: $\hat{F}_0 = 1 \rightarrow \hat{F}(\hat{t}) = \hat{A} \cdot \cos(\hat{\omega} \cdot \hat{t}) + 1$, the following solutions' map of $\hat{p}ull$ was obtained:

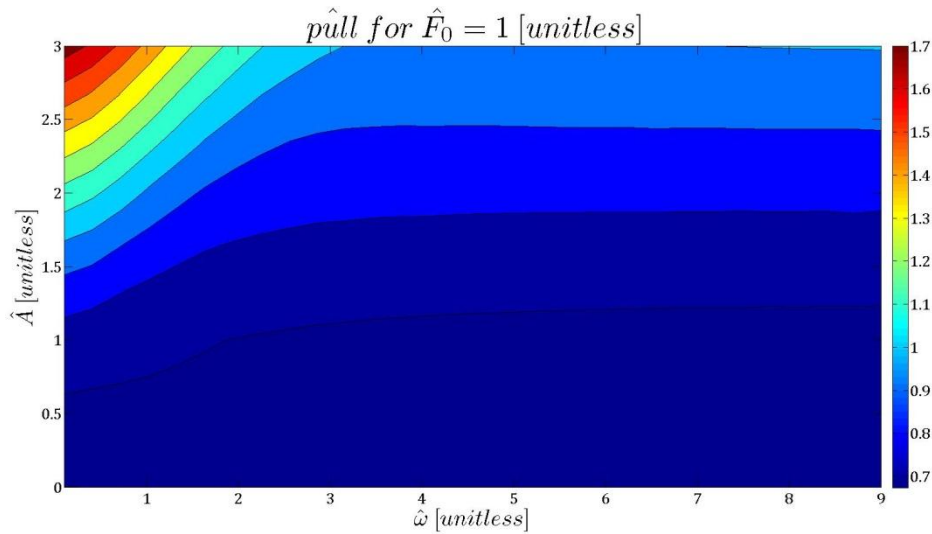


Figure 3-1 $\hat{p}ull$ for $\hat{F}_0 = 1$, $\hat{A} \in 0 - 3$, $\hat{\omega} \in 0 - 9$

An important fact being confirmed by these results was the non-linearity of the calculated metric $\hat{p}ull$ with the model's non-dimensional parameters.

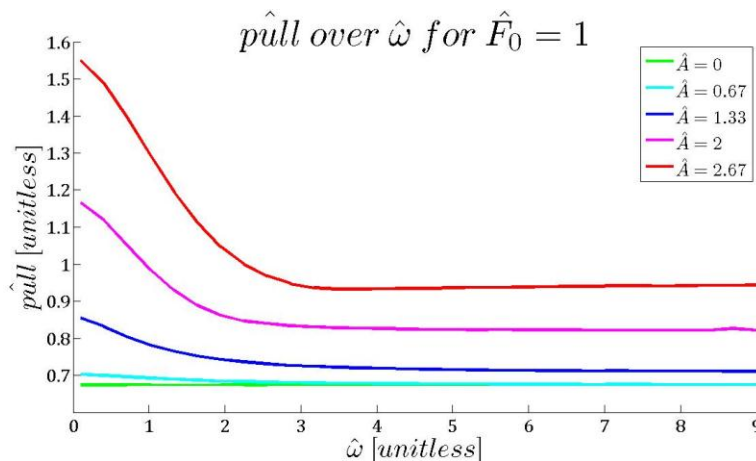


Figure 3-2 $\hat{p}ull$ for $\hat{F}_0 = 1$, $\hat{A} = 0, 0.67, 1.33, 2$ and 2.67 , $\hat{\omega} \in 0 - 9$

The same results from [Figure 3-1](#) were differently represented in [Figure 3-2](#), which emphasises the fact that a higher amplitude \hat{A} makes the oscillating frequency $\hat{\omega}$ more determinant to the metric $\hat{p}ull$.

3.2 With fixed force amplitude

For the particular case of: $\hat{A} = 3 \rightarrow \hat{F}(\hat{t}) = 3 \cdot \cos(\hat{\omega} \cdot \hat{t}) + \hat{F}_0$, a different map of solutions for \widehat{pull} was obtained:

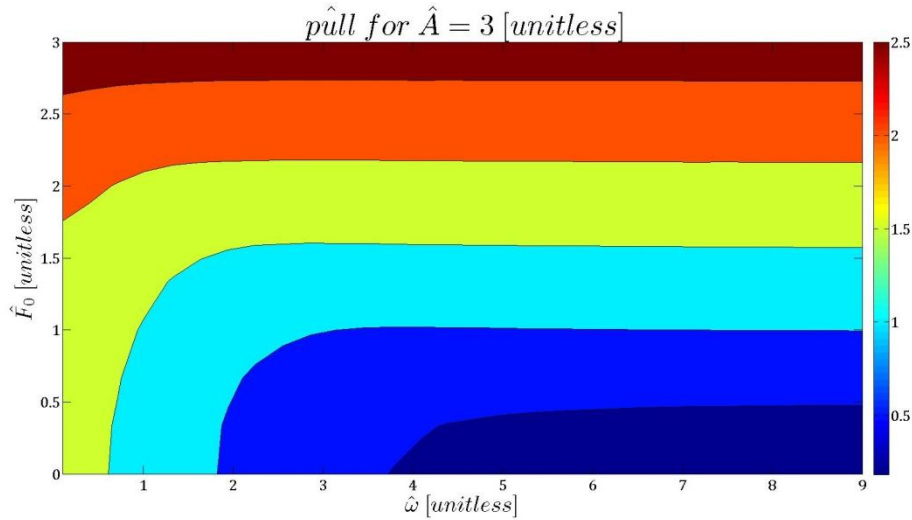


Figure 3-3 \widehat{pull} for $\hat{A} = 3$, $\hat{F}_0 \in 0 - 3$, $\hat{\omega} \in 0 - 9$

In this case it was observed that as the average force \hat{F}_0 approaches the fixed value of the force amplitude, the oscillating frequency becomes less significant to the transduced force \widehat{pull} .

From the 1D results presented in this chapter, it can be concluded that for driving forces with high amplitude \hat{A} , when compared to its average value \hat{F}_0 , the oscillating frequency $\hat{\omega}$ is an important and non-linear factor when determining the transduction of the flow induced wall shear stress in the luminal surface of the glycocalyx to the biomechanical force in the endothelial cell surface. This effect is probably due to the fact that the fibres of the cell attached glycocalyx oscillate around the vertical position, and becomes more significant in the range $\hat{\omega} \in [0 \ 4]$, in which the system is able to respond to the higher oscillation (the rod's oscillating amplitude resembles more the one of the driving force).

4 The two dimensional model

Having explored the importance of the frequency response of the 1D model of the glycocalyx, the next step was to post-process a larger, more realistic set of shear stress data. Although this larger set of data was three dimensional, simplifications described in 2.1 Model discussion allowed to post-process it using a two dimensional (2D) model. In other words, since interactions between adjacent rods were not considered, each one could be processed regardless of its position and orientation. Hence, an extension of the previous model to 2D was discussed and mathematically defined.

4.1 Model discussion and system of governing equations

When extending the model to 2D, two different ideas, here identified as A and B, arose:

- A) Replicating the same 1D model in the perpendicular direction: Model A, better described with the coordinate system in Figure 4-1 (θ_1, θ_2), adds to the model another rotational spring with equal properties but different orientation: its axis is also in the horizontal plane but was set perpendicular to the existing one's. Mechanically, the force in each direction loads the correspondent rotational spring and makes the rod turn in one of the coordinate system's angles.
- B) Allowing the 1D model to rotate: Model B is more easily characterised using the coordinate system in Figure 4-2 (θ, Φ). Instead of a rotational spring, it adds a free bearing in the vertical axis to allow the group "rod and rotational spring" turn with no other impediment than the drag caused by the rotation. Mechanically, the radial component of the force causes the rod to "bend" down and the orthogonal one makes it turn around. A schematic representation of this model is shown in Figure 4-3.

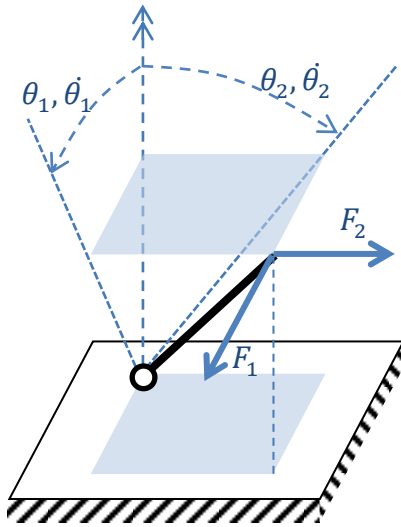


Figure 4-1 Coordinate system for Model A

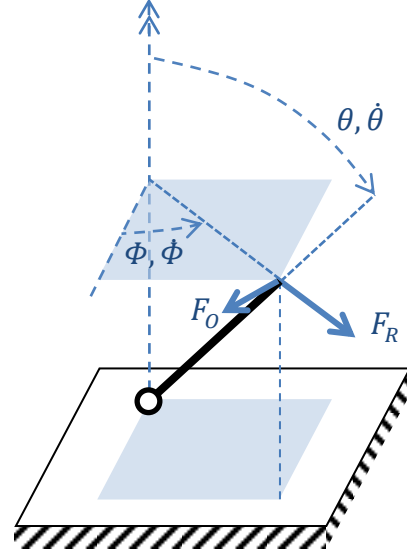


Figure 4-2 Coordinate system for Model B

The equivalence between these coordinate systems can be calculated using equations (Eq 4-1) to (Eq 4-4):

$$\theta_1 = \arccos\left(\frac{\cos(\theta)}{\sqrt{\cos^2(\theta) + \cos^2(\Phi) \cdot \sin^2(\theta)}}\right) \quad (\text{Eq 4-1})$$

$$\theta_2 = \arccos\left(\frac{\cos(\theta)}{\sqrt{\cos^2(\theta) + \sin^2(\Phi) \cdot \sin^2(\theta)}}\right) \quad (\text{Eq 4-2})$$

$$\theta = \arccos\left(\frac{\cos(\theta_1) \cdot \cos(\theta_2)}{\sqrt{\cos^2(\theta_1) + \sin^2(\theta_1) \cdot \cos^2(\theta_2)}}\right) \quad (\text{Eq 4-3})$$

$$\phi = \arccos\left(\frac{\sin(\theta_1) \cdot \cos(\theta_2)}{\sqrt{\sin^2(\theta_1) \cdot \cos^2(\theta_2) + \sin^2(\theta_2) \cdot \cos^2(\theta_1)}}\right) \quad (\text{Eq 4-4})$$

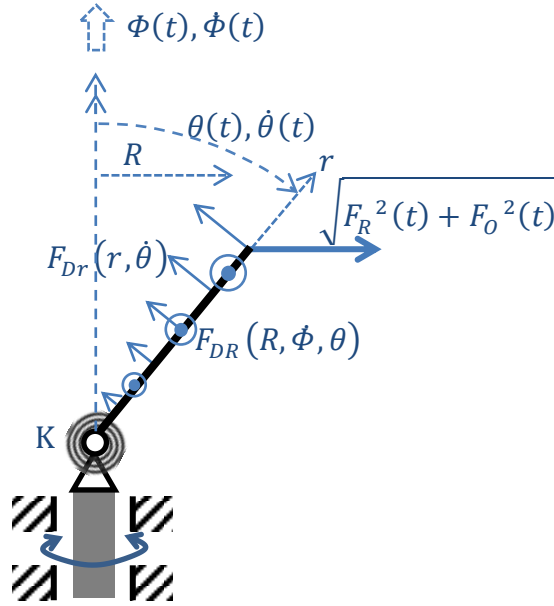


Figure 4-3 2D model B diagram

Each model, A and B, is mathematically expressed by a system of coupled non-linear differential equations. These are shown in equations (Eq 4-5) and (Eq 4-6) respectively:

$$\begin{cases} C \cdot \dot{\theta}_1(t) + K \cdot \theta_1(t) = F_1(t) \cdot \cos(\theta_1(t)) \cdot L \\ C \cdot \dot{\theta}_2(t) + K \cdot \theta_2(t) = F_2(t) \cdot \cos(\theta_2(t)) \cdot L \end{cases} \quad (\text{Eq 4-5})$$

$$\begin{cases} C \cdot \dot{\theta}(t) + K \cdot \theta(t) = F_R(t, \Phi(t)) \cdot \cos(\theta(t)) \cdot L \\ \zeta \cdot \dot{\Phi}(t) = F_O(t, \Phi(t)) \cdot L \end{cases} \quad (\text{Eq 4-6})$$

In (Eq 4-6), ζ is the coefficient of rotational friction around the vertical axis, and is calculated integrating the drag torque $F_{DR} \cdot R$ through the length of the rod (Eq 4-7) and (Eq 4-8).

$$F_{DR}(R, \dot{\Phi}, \theta) = \frac{\pi \cdot \mu \cdot \dot{\Phi} \cdot R \cdot \sin \theta}{c} \cdot \frac{r_f^2}{K_p} \quad (\text{Eq 4-7})$$

$$\zeta = \frac{1}{\dot{\Phi}} \int_0^L F_{DR}(R, \dot{\Phi}, \theta) \cdot R \cdot dR = \frac{L^3 \cdot \pi \cdot \mu \cdot r_f^2}{3 \cdot c \cdot K_p} \cdot \sin(\theta) = C \cdot \sin(\theta) \quad (\text{Eq 4-8})$$

Equation (Eq 4-6) can be therefore expressed as in (Eq 4-9), emphasising the fact that the governing system of equations is in fact coupled. There is no coordinate system for which these equations are not coupled.

$$\begin{cases} C \cdot \dot{\theta}(t) + K \cdot \theta(t) = F_R(t, \Phi(t)) \cdot \cos(\theta(t)) \cdot L \\ C \cdot \sin(\theta(t)) \cdot \dot{\Phi}(t) = F_O(t, \Phi(t)) \cdot L \end{cases} \quad (\text{Eq 4-9})$$

Whilst F_1 and F_2 do only depend on t , F_R and F_O do also depend on the rod's orientation, since they are the projection of the applied force on Φ 's and its orthogonal directions respectively.

Despite both models seemed to be reasonably suitable to simulate the mechanical behaviour of the glycoalyx, model A was found to react unequally to forces with the same magnitude but different orientation. As can be easily inferred from [Figure 4-4](#), when applying an arbitrary static torque of 1 N·m in the vertical plane of $\Phi = 0^\circ$ or $\Phi = 45^\circ$, the rod would rotate down $\theta = 85^\circ$ and $\theta = 70^\circ$ respectively. This was obviously an unwanted behaviour and therefore, Model B was chosen to study the mechanical response of the glycoalyx in 2D.

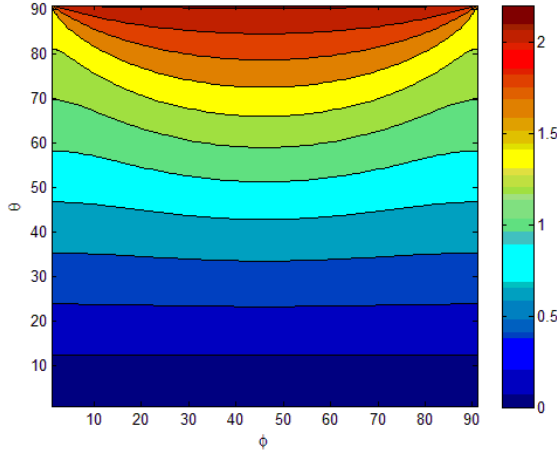


Figure 4-4 Spring-back torque of Model A for different angles θ and Φ

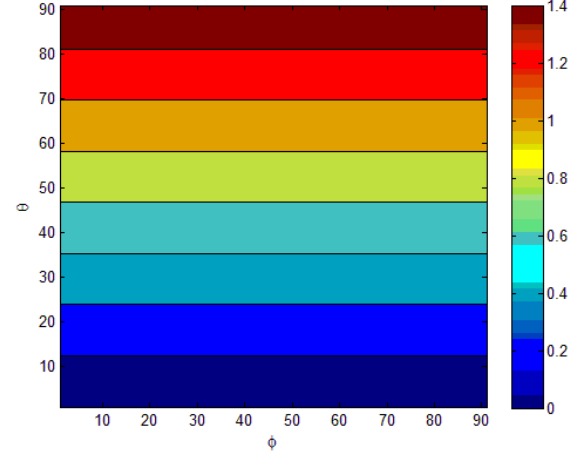


Figure 4-5 Spring-back torque of Model B for different angles θ and Φ

The system of governing equations ([Eq 4-6](#)) was then non-dimensionalised using the same parameters as in the 1-D model, i.e. ([Eq 2-13](#)) to ([Eq 2-15](#)), consequently leading to ([Eq 4-10](#)).

$$\begin{cases} \dot{\theta}(\hat{t}) + \theta(\hat{t}) = \widehat{F}_R(\hat{t}, \Phi(\hat{t})) \cdot \cos(\theta(t)) \\ \sin(\theta(\hat{t})) \cdot \dot{\Phi}(\hat{t}) = \widehat{F}_O(\hat{t}, \Phi(\hat{t})) \end{cases} \quad (\text{Eq 4-10})$$

4.2 Numerical solution and post-processing

The data to be processed consisted in a large set of points for each of which a sub-set of 3D vectors representing direction and magnitude of the shear stress at each time step were provided (see [5 Study of simulated shear stress in a rabbit's blood vessel](#)). Because of the definition of shear stress, all vectors corresponding to the same point's data were contained in the surface's tangent plane at that particular point, thus allowing for a 2D post-processing. However, the mentioned data format required a slightly different but equally simple approach when post-processing it: the vector with higher magnitude, $\overrightarrow{F(n)}$, defined $\Phi = 0$, whilst the immediately following one, $\overrightarrow{F(n+1)}$, defined the positive direction (see [Figure 4-6](#)). Then, each 3-D vector $\overrightarrow{F(t)}$ could be converted through ([Eq 4-11](#)) into a magnitude and an angle, easily projectable to F_R and F_O . The origin and positive direction of the coordinate Φ does have no effect on the result "pull".

$$\Phi_{force}(\overrightarrow{F(t)}) = \frac{\arccos(\overrightarrow{F(t)} \cdot \overrightarrow{F(n)})}{|\overrightarrow{F(t)}| \cdot |\overrightarrow{F(n)}|} \quad (\text{Eq 4-11})$$

Notes on ([Eq 4-12](#)): Computationally, a different formula employing $\arctan\left(\frac{\overrightarrow{F(t)} \times \overrightarrow{F(n)}}{\overrightarrow{F(t)} \cdot \overrightarrow{F(n)}}\right)$ was used in order to reach higher accuracy in angles near the origin. Also, further calculations to provide the adequate result within the range $0 - 2\pi$ were performed. Using as $\overrightarrow{F(n)}$, the vector $\overrightarrow{F(t)}$ with highest magnitude was intended to enhance computational accuracy too.

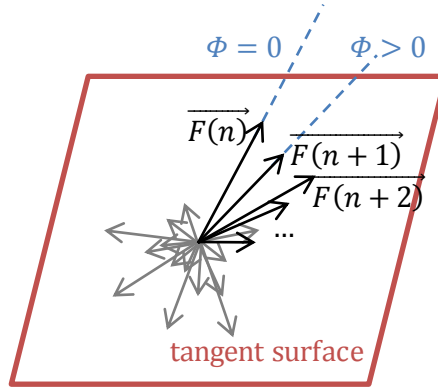


Figure 4-6 Adaptive coordinate Φ origin and positive direction for the 2-D model

Accordingly, the initial conditions for the 2D IVP were calculated using equations (Eq 4-12) and (Eq 4-13):

$$\widehat{F(0)} \cdot \cos(\beta_\theta) = \beta_\theta \implies \beta_\theta \quad (\text{Eq 4-12})$$

$$\beta_\Phi = \Phi_{force}(\widehat{F(0)}) \quad (\text{Eq 4-13})$$

The solving algorithm did not differ from the 1D one (see 2.6 Numerical solution) in any other way than the above described method to calculate the driving force and the system of coupled non-linear differential equations itself.

The post-processing was also very similar to that performed in the 1D model, ensuring the correct calculation of the “ \widehat{pull} ” numeric:

$$\widehat{F}_p(\hat{t}) = \widehat{F}_R(\hat{t}, \Phi(\hat{t})) \cdot \sin(\theta(\hat{t})) \quad (\text{Eq 4-14})$$

$$\widehat{Pull} = \sum_{n=0}^{n_m} \int_{\hat{t}=\hat{t}_s+\hat{t}_{2n}}^{\hat{t}=\min\{\hat{t}_s+\hat{t}_{2n+1}, \hat{t}_s+T\}} \widehat{F}_p(\hat{t}) \cdot d\hat{t} \quad (\text{Eq 4-15})$$

$$\widehat{pull} = \frac{\widehat{Pull}}{\widehat{F}} \quad (\text{Eq 4-16})$$

(Eq 4-15) uses the same nomenclature than (Eq 2-21). $[\hat{t}_s + \hat{t}_{2n} \quad \hat{t}_s + \hat{t}_{2n+1}]$. However, in this case it refers to the intervals of \hat{t} for which $\widehat{F}_R(\hat{t}, \Phi(\hat{t})) > 0$, being such condition enough to ensure that a pulling force is integrated.

In order to validate the extension to 2D of the mechanical model for the glycocalyx, it was tested against the 1D model while working in different planes ($\Phi = 0, \frac{\pi}{6}, \frac{\pi}{4}, \frac{\pi}{2} \text{ rad}$) and with different values of the non-dimensional parameters.

5 Study of simulated shear stress in a rabbit's blood vessel

The 2D model had been prepared to post-process simulated data from a 3D geometry, with which more realistic results and conclusions could be obtained. Before presenting the results of such study, though, considerations regarding the original data and the different cases considered are made in the following section:

5.1 Original data and previous considerations

The larger set of data had previously been obtained by Peiffer et al. [17] from a simulation of the blood flow in a rabbit's aortic arch and descending thoracic aorta. Time dependant wall shear stress magnitude and direction over a period of the pulsatile flow ($T = 0.32\text{ s}$) were provided for over 665,000 points wisely distributed across the geometry. Figure 5-1 shows the evolution of the shear stress magnitude in an arbitrary point over a period and Figure 5-2 shows the blood pressure in the described geometry at an arbitrary moment of the period.

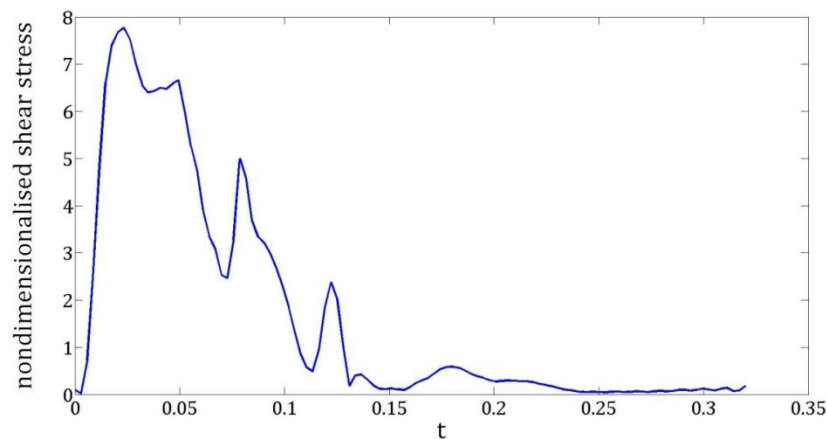


Figure 5-1 Non-dimensionalised shear stress evolution over a period T in a particular point (source: Peiffer et al. [17])

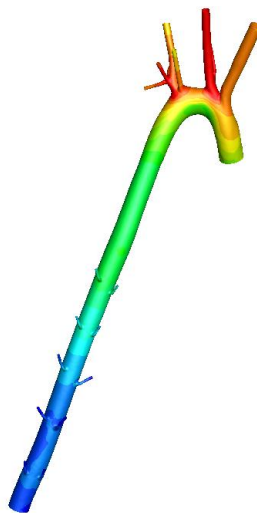


Figure 5-2 Geometry of a rabbit's aortic arch and descending thoracic aorta (pattern: blood pressure) (source: Peiffer et al. [17])

Using the approach explained in 4.2 Numerical solution and post-processing, the transduced force was calculated ($\tau[Pa] \rightarrow \hat{\tau}[Pa] \xrightarrow{\text{glycocalyx}} \widehat{pull} \rightarrow pull$) and compared to the average shear stress over the period ($\bar{\tau}$).

Firstly, a much reduced set of 11 points was chosen both to check the model and to extract the first conclusions. Secondly, a larger set of τ -data corresponding to a cropped section of the geometry (including over 70,700 points, that is 10% of the whole set) was also studied. This cropped geometry corresponds to a region of the descending thoracic aorta including two intercostal branches. In both studies, different combinations of the glycocalyx defining parameters (including the baseline case) were considered.

In the non-dimensionalisation defined by (Eq 2-13) to (Eq 2-15), two dimensional reference magnitudes had been used: the reference time (RT [s]) (Eq 5-1), and the reference force (RF [N]). The latter is expressed in (Eq 5-2) as reference shear stress ($RSS = N \cdot RF$ [Pa]). These reference magnitudes account for the glycocalyx properties in the non-dimensional model.

$$RT = \frac{K}{C} = \dots \approx 3 \cdot \frac{G}{L^2} \cdot \frac{K_p}{\mu} \quad (\text{Eq 5-1})$$

$$RSS = N \cdot \frac{K}{L} \approx G \quad (\text{Eq 5-2})$$

Note that, from (Eq 2-13), (Eq 2-15), (Eq 5-1) and (Eq 5-2) $\hat{t} = \frac{t}{RT}$ and $\hat{F} = \frac{\tau}{RF} = \frac{\tau}{RSS}$. Therefore $\hat{F}(t/RT) = \frac{\tau(t)}{RSS}$. Equivalently, one can re-dimensionalise as follows: $pull$ [Pa] = $pull \cdot RSS$.

It was assumed that from the parameters in (Eq 5-1), G and L were likely to vary from one region of the endothelial cell membrane to another. Therefore, the boundary values of G and a higher length L were also studied. On the other hand, K_p and μ were thought to remain constant across the vascular system. Then, the following table for RT and RSS was calculated:

$K_p = 3.37 \cdot 10^{-19} m^2$ $\mu = 1.6 \cdot 10^{-3} Pa \cdot s$	$L = 70 nm$	$L = 100 nm$
$G = 10.0 Pa$	$RT \approx 1.288 s$ $RSS \approx 10.0 Pa$	$RT \approx 0.013 s$ $RSS \approx 10 Pa$
$G = 6.7 Pa$	$RT \approx 0.863 s$ $RSS \approx 6.7 Pa$	$RT \approx 0.026 s$ $RSS \approx 6.7 Pa$
$G = 3.4 Pa$	$RT \approx 0.438 s$ $RSS \approx 3.4 Pa$	$RT \approx 0.039 s$ $RSS \approx 3.4 Pa$

Table 5-1 Time and Force scales for different values of glycocalyx' shear modulus and length. Baseline case parameters highlighted in blue

Figure 5-3 helps visualising the dependence of the reference time (RT) on variables G and L (for fixed values of K_p and μ):

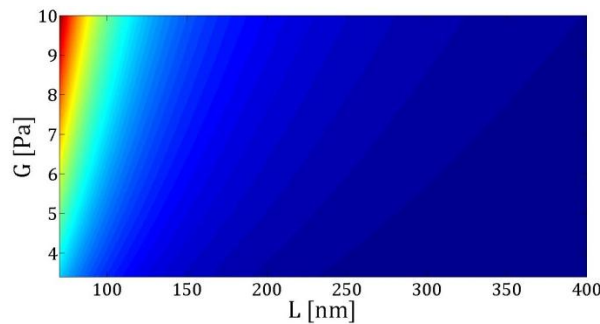


Figure 5-3 Reference time (RT) dependence on G and L with fixed μ and k_p

5.2 Analysis of specific data points

The solving algorithm was run with the values presented in Table 5-1, in 11 points (labelled 1 to 11). In each case, \widehat{pull} was compared with the average shear stress ($\hat{\tau} = \frac{1}{\hat{T}} \cdot \int_{\hat{t}_a}^{\hat{t}_a + \hat{T}} \hat{\tau} \cdot d\hat{t}$) using the ratio $\frac{\hat{\tau}}{\widehat{pull}}$. Figures in Table 5-2 show the ratio $\frac{\hat{\tau}}{\widehat{pull}}$ for each of these cases (note vertical scale varies from one figure to another).

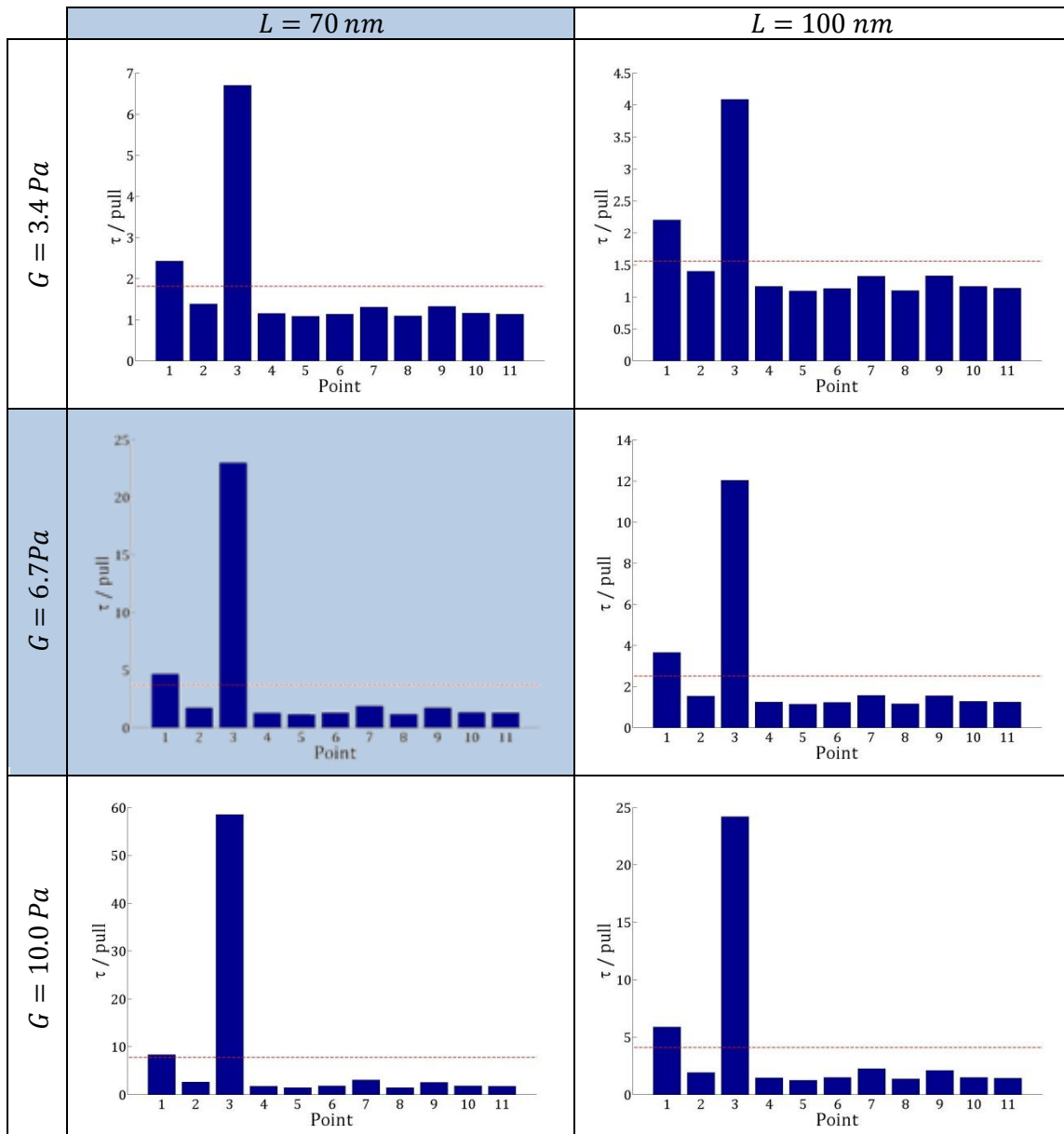


Table 5-2 average shear stress $\hat{\tau}$ over \widehat{pull} ratio in 11 points for each case presented in Table 5-1

There were two important conclusions to obtain from the results in Table 5-2:

- It was obvious that the ratio of the two metrics was different in different points. That implied what was already known from the 1D model results: both the importance of the frequency response and the nonlinearity of the model resulted in a different effect of the shear stress to the endothelial cell surface from the previously considered in the matter.
- Furthermore, the nonlinearity of the model did also cause the difference of this ratio between different points to vary depending on the time and force scales. For instance, considering the ratio for points 1 and 2 one can see how its difference changes between different cases.

Although these conclusions could make one think that the two patterns of $\bar{\tau}$ and $pull$ would indeed differ, it was important to realise that it could also be the case that smaller differences between both patterns, such as sharpening or smoothing would be obtained.

5.3 2D model results in the 3D geometry

Results presented in this section, both $\bar{\tau}$ and $pull$, were re-dimensionalised to $[Pa]$. Scales vary only from the front- to the rear-view images.

In the studied region, the average wall shear stress $\bar{\tau}$ $[Pa]$ had the distribution showed in Figure 5-4, whilst, for the baseline case of reference dimensions, the distribution of $pull$ $[Pa]$ was found to be the one shown in Figure 5-5.

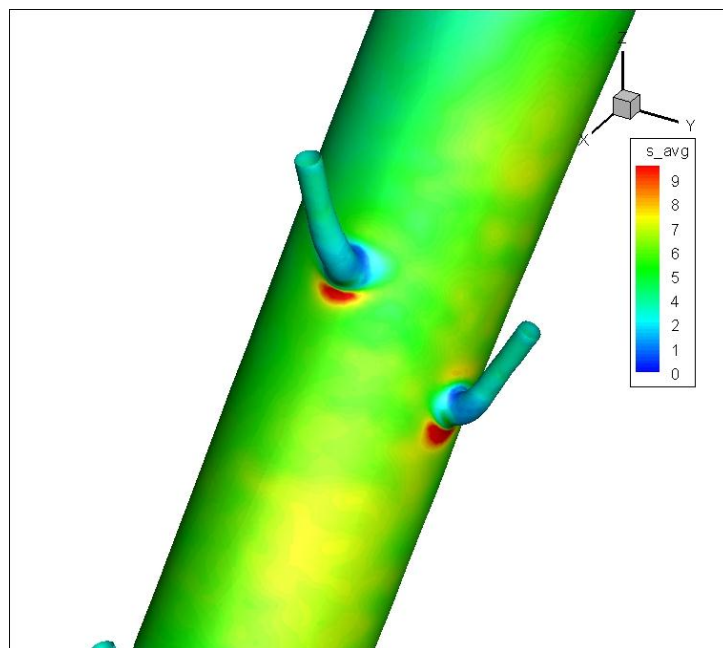


Figure 5-4 Average shear stress ($\bar{\tau}$ $[Pa]$) distribution in the studied region.

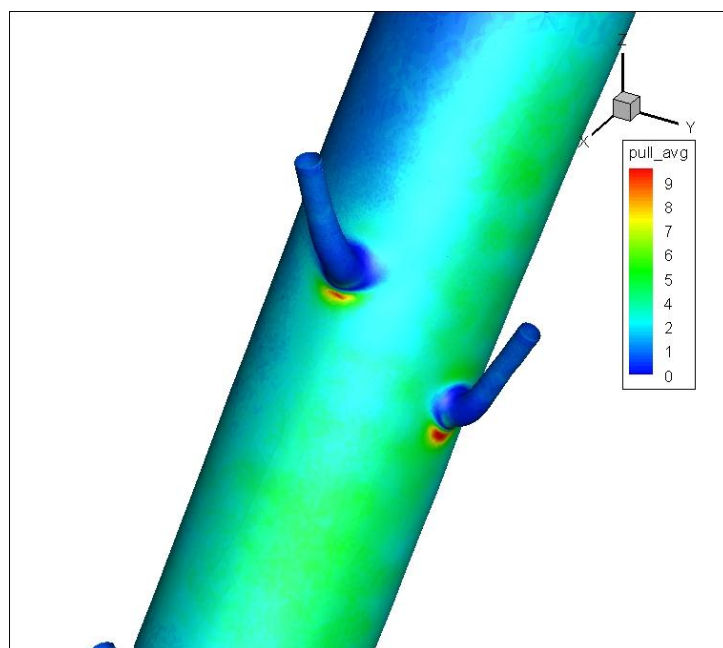


Figure 5-5 Transduced fluid induced shear stress through the glycocalyx to the endothelial cell surface ($pull$ $[Pa]$). Distribution for the baseline case ($G = 6.7 Pa, L = 70 nm$)

Again, the same analysis was performed for different reference time and shear stress (corresponding to different glycocalyx parameters' combinations, see [Table 5-1](#) in [Error! Reference source not found. Error! Reference source not found.](#)).

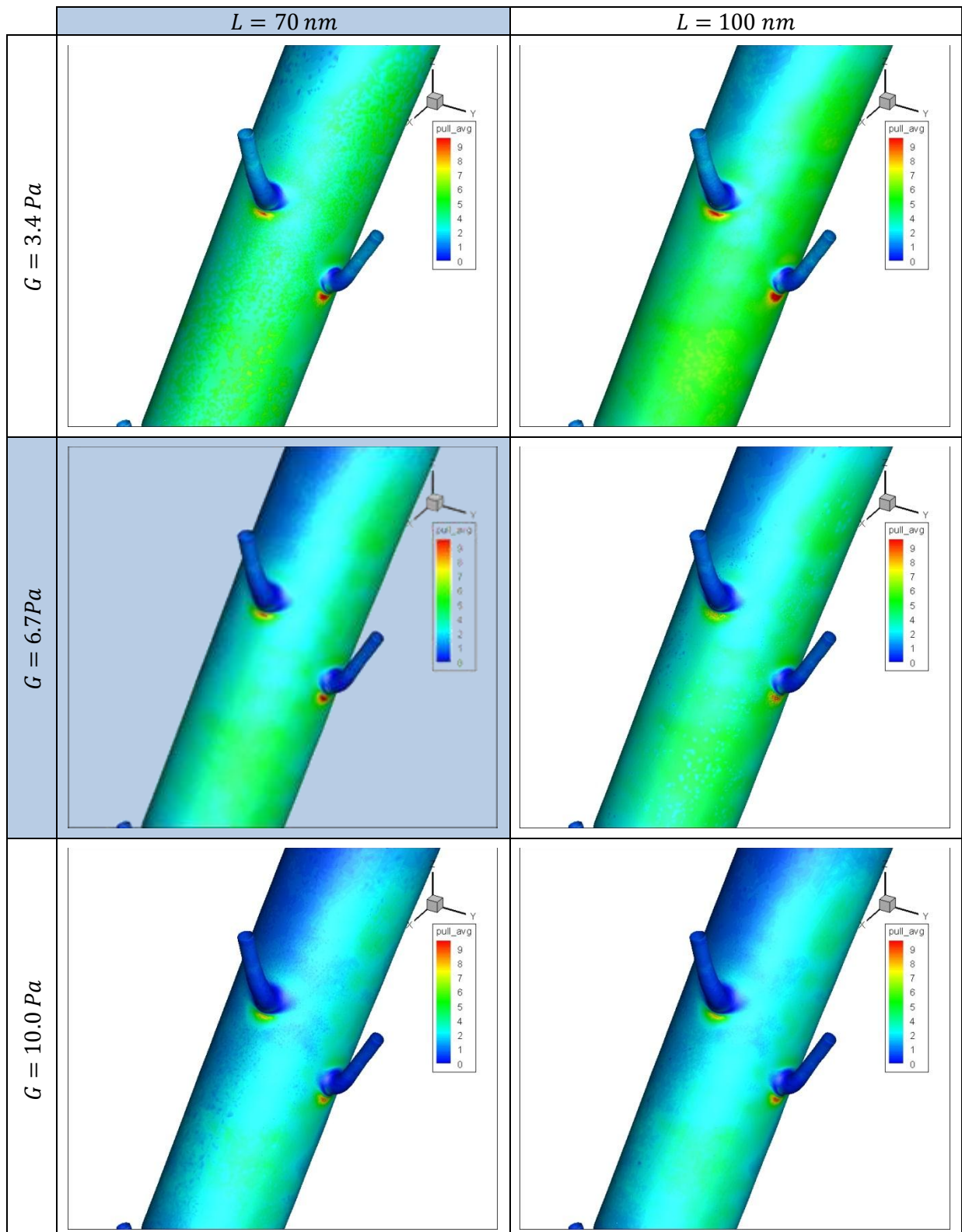


Table 5-3 $pull [Pa]$ for each case presented in Table 5-1 Time and Force scales for different values of glycocalyx' shear modulus and length. Baseline case parameters highlighted in blue

The rear view of the same results is shown in [Figure 5-6](#) (average wall shear stress $\bar{\tau}$ [Pa]) and [Figure 5-7](#) (*pull* [Pa]). Note that the scale is different from the front view results.

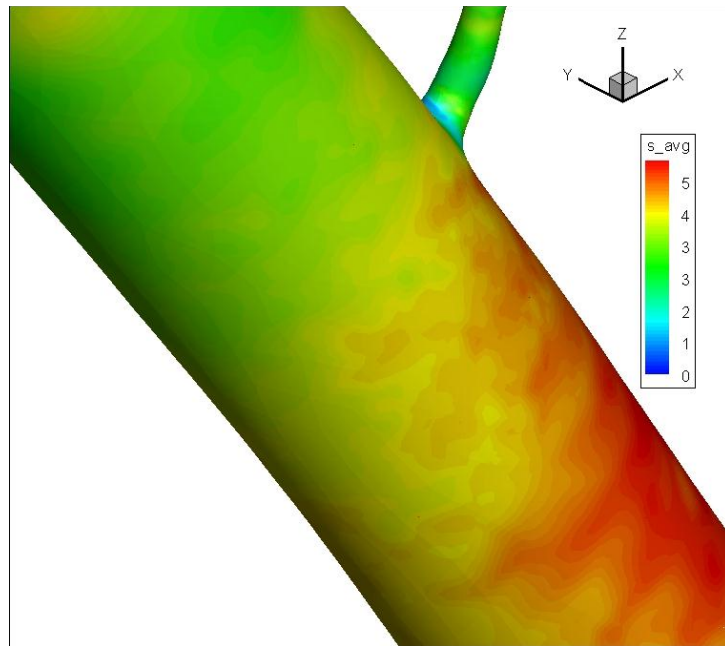


Figure 5-6 Average shear stress ($\bar{\tau}$ [Pa]) distribution in the studied region (rear view)

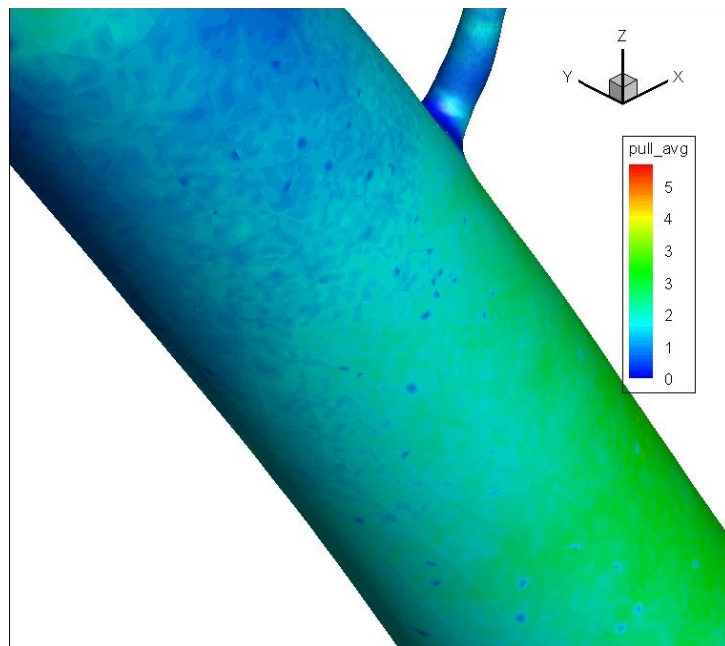


Figure 5-7 Transduced fluid induced shear stress through the glycocalyx to the endothelial cell surface (*pull* [Pa]). Distribution for the baseline case ($G = 6.7$ Pa, $L = 70$ nm) (rear view)

And the rear view of the resulting $pull$ [Pa] for the different cases studied:

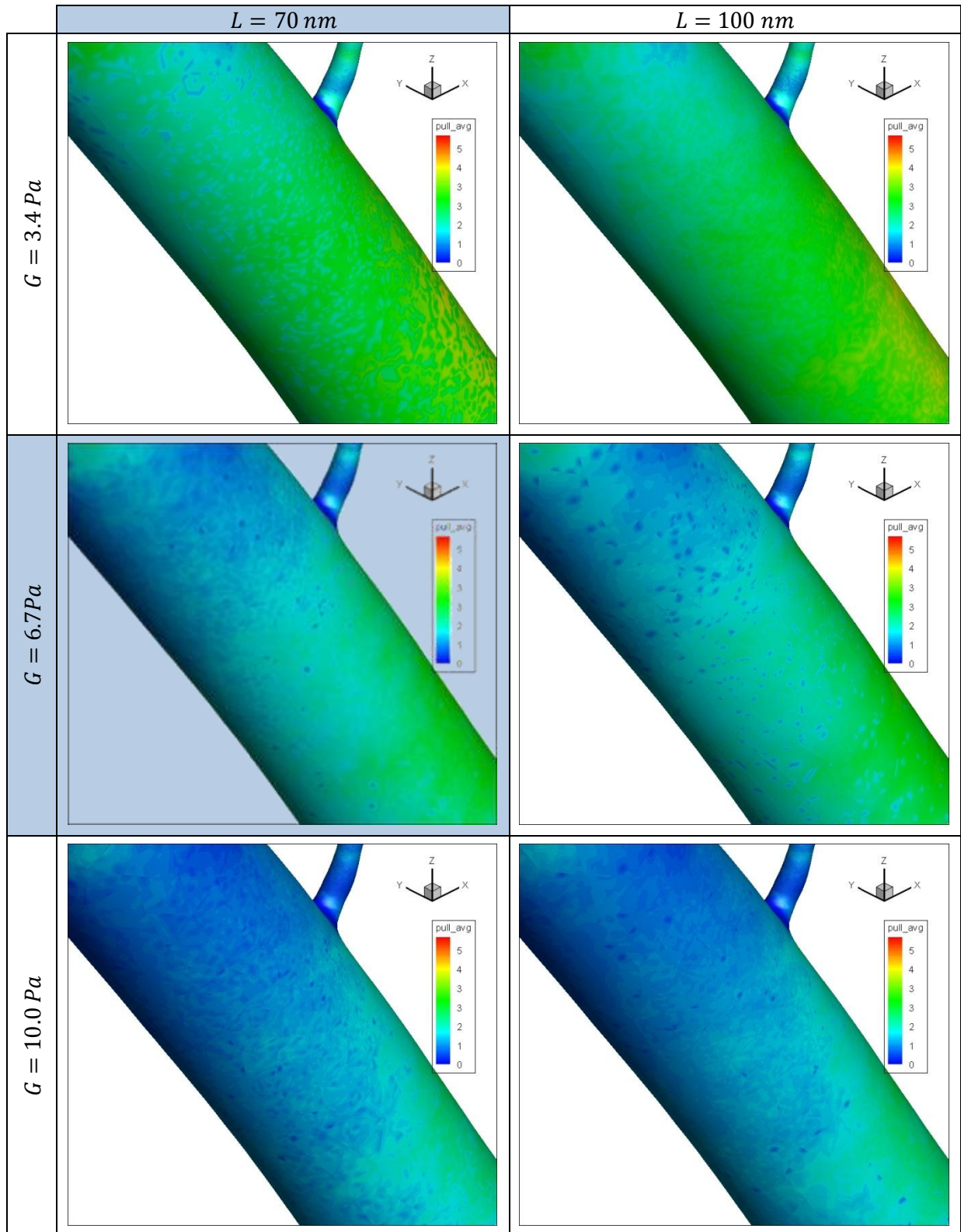


Table 5-4 $pull$ [Pa] for each case presented in Table 5-1 (rear view)

The presented results showed that, despite the previous findings, patterns of average shear stress $\bar{\tau}$ and *pull* show no major differences. Analysing data from 10 arbitrary chosen points in was confirmed that non-linear changes of the ratio $\frac{\bar{\tau}}{pull}$ presented in the previous section were still happening:

Point	1	2	3	4	5	6	7	8	9	10
$\bar{\tau}$ [Pa]	3.93	5.35	3.58	0.95	12.18	9.08	6.81	4.84	6.63	12.65
<i>pull</i> [Pa]	1.11	2.68	1.38	0.20	9.23	6.06	4.04	2.04	3.77	9.99
$\frac{\bar{\tau}}{pull}$	3.54	2.00	2.59	4.75	1.32	1.50	1.69	2.37	1.76	1.27

Table 5-5 $\bar{\tau}$ over *pull* ratio for 10 arbitrary points of the studied geometry

This lack of major differences between the compared patterns could be in part due to the little variation of the frequency of the pulsatile-flow-originated wall shear stress across the geometry (see Figure 5-8), which leads to a re-scaling of the shear stress. This re-scaling, although non-linear, would not lead to important changes in the pattern of the ‘felt’-shear stress.

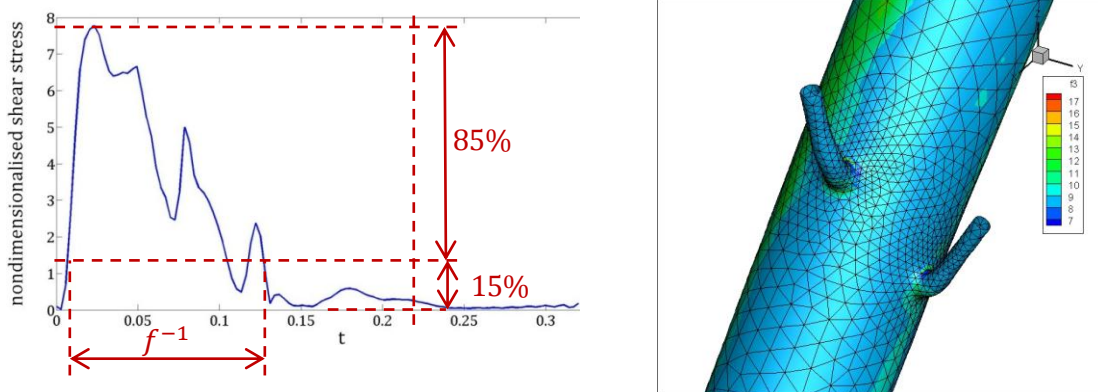


Figure 5-8 Approximate frequency [Hz] of the oscillation of the shear stress

Figure 5-8 (left) describes the approximate calculation of the temporal frequency of the shear stress oscillation. It is mentioned in 6.2 Future research that a spectral analysis, probably using the fast Fourier transform would be desirable.

There is certainly a difference, though, on the amount of shear stress transferred through the glycocalyx to the endothelial cell membrane depending on the glycocalyx layer’s characteristics. It turns out both from Table 5-3 and Table 5-4 that a higher shear modulus, which means stiffer fibres, leads to fewer force transduction. Not as much visible is a similar effect with the fibres’ length: it can also be inferred from the presented results that longer fibres transfer more force to the endothelium. Mechanically, both effects are related to the angle turned by the rod modelling the fibres: while a longer rod leads to a higher torque, a less stiff fibre implies that a higher turning angle is reached for the same torque. In both cases, the same force would bend the rod further down, reaching a higher alignment with it and transferring more force through it.

However, the calculated metric *pull* resulted in a negative value for a small number of points (in fact, for less than 1‰ of the points processed). Such results are fundamentally incorrect, because by definition *pull* must be positive; otherwise it makes no sense physically. Since its cause remains unknown, and is probably due to a bug in the code, the author of this dissertation must refer to future research work to double check (and if necessary, correct) the above presented results.

6 Conclusions and future research

6.1 Conclusions

A mechanical model of the glycocalyx was developed in accordance with the literature on the matter. For this model, the glycocalyx' inertia was found to be negligible when compared to drag- and stiffness-induced forces.

A convenient mathematical expression allowed defining, coding and checking a MATLAB algorithm that calculated the glycocalyx' response and a new metric called *pull*. This was defined, for a given oscillating driving force, as the actual average pulling force transferred through the glycocalyx to the endothelial cell surface. This new metric would then be compared to the average driving force (or equivalently to the average shear stress $\bar{\tau}$).

From the 1D analysis of idealised, sinusoidal driving forces it was concluded that for driving forces with high amplitude, when compared to its average value, the oscillating frequency is a key, non-linear factor when determining *pull*. This effect was increasingly important as the oscillating frequency decreased, allowing the system to respond effectively to the higher amplitude.

The 1D mechanical model of the glycocalyx was appropriately extended to 2D in order to study simulated shear stress data from a 3D geometry, corresponding to the descending thoracic aorta of a rabbit. From the surface analysis of this large data set, comparing *pull* and $\bar{\tau}$, it was concluded that although no major differences between the two metrics were observed, the glycocalyx does certainly play a role in determining the amount of force transferred to the endothelium. Both higher length of its fibres (a thicker cell-attached glycocalyx layer) and less stiff fibres resulted in higher amounts of transduced force. It was also hypothesised that the lack homogeneity of shear stress oscillation frequency across the geometry could cause the pattern of *pull* to be so similar to the $\bar{\tau}$'s one.

6.2 Future research

In the near future, the presented model could be double-checked and improved, although that would probably lead to a model with increased complexity. Some of these next-steps are summarised below:

- As pointed out in [5.3 2D model results in the 3D geometry](#), a further check of the results with special attention to the very few cases in which the calculated metric *pull* results in a negative value is needed.
- Given that the limitation in time of this project did not allow post-processing the entire set of data available (see [5.3 2D model results in the 3D geometry](#)), the first 'next thing to do' would be it. That would also allow for a more in-depth analysis of the results and the importance of the frequency response of the glycocalyx to the pulsatile blood flow.
- It would be also desirable to present results as in [Figure 1-2](#) (source: Vincent et al. [8]), for which a 'computational incision' along the aortic wall to unwrap the geometry of the descending aorta was made.
- Solve the system of non-linear system of coupled differential equations with a different approach: assuming the response's oscillating frequency is the same as the perturbation's (driving force), it can be solved as a boundary values problem (BVP) instead of doing it as an IVP. That might increase the solution's accuracy. As mentioned in the [Acknowledgements](#) section, another student in the Department of Aeronautics of Imperial College London is already trying this new approach using University of Oxford's *chebfun* solver for MATLAB.
- The solving algorithms described in this dissertation have been coded in MATLAB and use this software's built-in solver *ode45*. However, the process takes a lot of time and in order to speed it

up, a wise option would be to code it in C++. Yet, that arises the problem of implementing a differential equation solver which, although feasible (in fact I did so to check ode45's accuracy with the specific nonlinearity featured by the presented model), that would likely lead to a decrease in accuracy. A different way to solve the model faster which was considered, but not explored, would be using spectral methods.

- Modelling the cell-attached glycocalyx' fibres as flexible bars as suggested by Han et al. [10].
- Although it has already been justified not having done so (see 2.1 Model discussion), one could consider the increment in stiffness when the fibres are stretched, described by M.I.T.'s PhD report by Yao [9] and shown in Figure 6-1. The change in the model described in this dissertation would be the one described by (Eq 6-1).

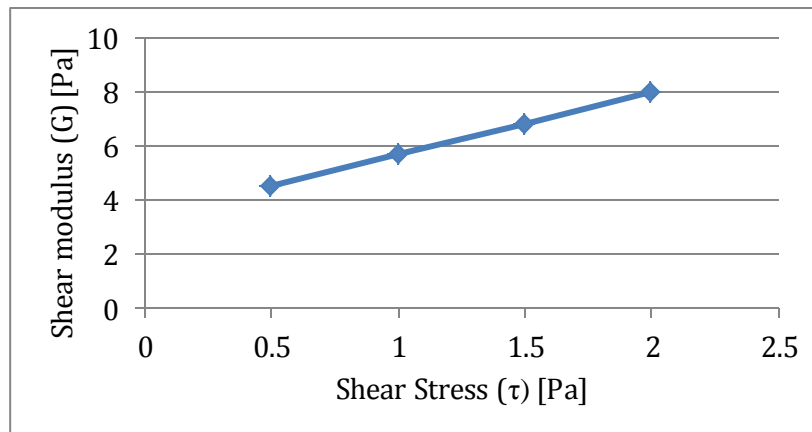


Figure 6-1 Glycocalyx' shear modulus dependence on applied shear stress (data source: Yao [9])

$$K(\tau) \approx \frac{L \cdot G(\tau)}{N} \quad (\text{Eq 6-1})$$

- Study of the variation of the shear stress frequency spectrum across the geometry of the aortic arch and descending thoracic aorta.

Nomenclature

1 Introduction

Glycocalyx	Endothelial Glycocalyx Layer, Endothelial Surface Layer
BHF	British Heart Foundation

2 The one dimensional model

1D	One dimensional
$\ddot{y}(x)$	Second derivative $\frac{d^2y(x)}{dx^2}$
$\dot{y}(x)$	First derivative $\frac{dy(x)}{dx}$
$\theta(t)$	Angle rotated down by the rod [<i>rad</i>]
I	Inertia of the rod [$kg \cdot m^2$]
C	Coefficient of rotational friction $\left[\frac{N \cdot m}{s \cdot rad}\right]$
m	Rod's mass [kg]
L	Rod's length [m]
r	Linear coordinate with the direction of the rod and origin at its articulation
F_D	Drag force with respect to θ rotation [N]
μ	Plasma viscosity [$Pa \cdot s$]
r_f	Fibre radius [m]
v_f	Fibre volume fraction [<i>unitless</i>]
K_p	Darcy permeability of the glycocalyx [m^2]
Δ	Fibre gap [m]
K	Coefficient of a torsion spring $\left[\frac{N \cdot m}{rad}\right]$
G	Shear modulus [Pa]
τ	Shear stress [Pa]
N	Number of rods per area unit $\left[\frac{1}{m^2}\right]$
$F(t)$	Driving force applied on top of each rod [N]
ω	Angular frequency [Hz]
T	Period [s]
A	Amplitude of the force [N]
F_0	Offset around which the force oscillates [N]
\hat{t}	Non-dimensional time [<i>unitless</i>]
$\hat{\omega}$	Non-dimensional frequency [<i>unitless</i>]
\hat{T}	Non-dimensional period [<i>unitless</i>]
\hat{A}	Non-dimensional amplitude [<i>unitless</i>]
\hat{F}_0	Non-dimensional offset [<i>unitless</i>]
IVP	Initial Value Problem
β	Initial condition $\theta(\hat{t} = 0)$ [<i>rad</i>]
Γ	Residual in the <i>Manufactured Solutions Method</i> [<i>unitless</i>]
$\hat{F}_p(\hat{t})$	Projection of the driving force in the direction of the rod [N] Tractioning $\hat{F}_p(\hat{t})$ integrated over a period T [<i>unitless</i>]. Its physical meaning
\widehat{Pull}	is the actual pulling force transferred through the glycocalyx to the endothelial cell surface
\widehat{pull}	\widehat{Pull} averaged over a period T [<i>unitless</i>]
n	Ascending integer number (0, 1, 2...) [<i>unitless</i>]
n_m	Value of n for which $\hat{t}_s + \widehat{t}_{2 \cdot (n_m + 1)} > \hat{T}$ [<i>unitless</i>]
\hat{t}_s	Arbitrary value of \hat{t} for which $\theta(\hat{t})$ has reached the steady state [<i>unitless</i>]
$[\hat{t}_s + \widehat{t}_{2n} \quad \hat{t}_s + \widehat{t}_{2n+1}]$	Interval of \hat{t} for which $\hat{F}(\hat{t}) \cdot \theta(\hat{t}) > 0$ [<i>unitless</i>]

4 The two dimensional model

2D	Two dimensional
θ_1	Rod's turned angle in xz-plane (from coordinate system A) [rad]
θ_2	Rod's turned angle in yz-plane (from coordinate system A) [rad]
θ	Rod's turned angle in Φ z-plane (from coordinate system B) [rad]
Φ	Rod's turned angle in xy-plane (from coordinate system B) [rad]
F_1	Driving force in x direction [N]
F_2	Driving force in y's direction [N]
F_R	Driving force in Φ 's direction [N]
F_O	Driving force in Φ 's orthogonal direction [N]
ζ	Coefficient of rotational friction $\left[\frac{N \cdot m}{s \cdot rad}\right]$ for Φ 's rotation
R	Linear coordinate within the horizontal plane, origin in the z-axis and direction Φ
$\frac{F_{DR}}{F(t)}$	Drag force with respect to Φ rotation [N]
$\overrightarrow{F(t)}$	Vector representing magnitude and direction of a driving force at t [N]
$\overrightarrow{F(n)}$	Vector of a $\overrightarrow{F(t)}$ set with maximum magnitude.
β_θ	Initial condition $\theta(\hat{t} = 0)$ [rad]
β_Φ	Initial condition $\Phi(\hat{t} = 0)$ [rad]
Φ_{force}	$\overrightarrow{F(t)}$ orientation in Φ coordinate

5 Study of simulated shear stress in a rabbit's blood vessel

RT	Reference time (used in the nondimensionalisation) [s]
RF	Reference force (used in the nondimensionalisation) [N]
RSS	Reference shear stress, equivalent to the reference fore ($RSS = N \cdot RF$), (used in the nondimensionalisation) [Pa]

6 Conclusions

BVP	Boundary Values Problem
-----	-------------------------

Bibliography

- [1] M. Nieuwdrop, M. C. Meuwese, H. L. Mooij, C. Ince, L. N. Broekhuizen, J. J. P. Kastelein and E. S. G. Stries, "Measuring endothelial glycocalyx dimensions in humans: a potential novel tool to monitor vascular vulnerability," *Journal of Applied Physiology*, vol. 104, pp. 845-852, 2007.
- [2] A. Pries, T. Secomb and P. Gaehtgens, "The endothelial surface Layer," *Pflügers Archiv European Journal of Physiology*, pp. 653-666, 2000.
- [3] S. Reitsma, D. W. Slaaf, H. Vink, M. A. M. J. van Zandvoort and M. G. A. oude Egbrink, "The endothelial glycocalyx: composition, functions, and visualization," *Pflügers Archiv European Journal of Physiology*, vol. 454, pp. 345-359, 2007.
- [4] B. M. van den Berg, H. Vink and J. A. E. Spaan, "The Endothelial Glycocalyx Protects Against Myocardial Edema," *Circulation Research*, vol. 92, pp. 592-594, 2003.
- [5] S. Weinbaum, X. Zhang, Y. Han, H. Vink and S. Cowin, "Mechanotransduction and flow across the endothelial glycocalyx," *Proceedings of the National Academy of Sciences of the USA*, vol. 100, no. 13, pp. 7988-7995, 2003.
- [6] S. Weinbaum, J. M. Tarbell and E. R. Damiano, "The Structure and Function of the Endothelial Glycocalyx Layer," Annual Reviews, Boston, 2007.
- [7] A. M. Shaaban and A. J. Duerinckx, "Wall Shear Stress and Early Atherosclerosis: A review," *American Journal of Roentgenology*, vol. 174, no. 6, pp. 1657-1665, 2000.
- [8] P. E. Vincent, A. M. Plata, A. A. E. Hunt, P. D. Weinberg and S. J. Sherwin, "Blood flow in the rabbit aortic arch and descending thoracic aorta," *J. R. Soc. Interface*, pp. 1-12, 2011.
- [9] Y. Yao, "Three-dimensional Flow-induced Dynamics of the Endothelial Surface Glycocalyx Layer," Massachusetts Institute of Technology, Boston, 2007.
- [10] Y. Han, S. Weinbaum, J. A. E. Spaan and H. Vink, "Large-deformation analysis of the elastic recoil of fibre layers in a Brinkman medium with application to the endothelial glycocalyx," *Journal of Fluid Mechanics*, vol. 554, pp. 217-235, 2006.
- [11] T. Sadiq, S. Advani and R. Parnas, "Experimental investigation of transverse flow through aligned cylinders," *International Journal of Multiphase Flow*, vol. 21, no. 5, pp. 755-774, 1995.
- [12] A. S. Sangani and A. Acrivos, "Slow flow through a periodic array of spheres," *Int. J. Multiphase Flow*, vol. 8, no. 4, pp. 343-360, 1982.
- [13] M. Haidekker, A. Tsai, T. Brady and H. Stevens, "A novel approach to blood plasma viscosity measurement using fluorescent molecular rotors," *American Journal of Physiology, Heart and Circulatory Physiology*, vol. 282, p. H1609-H1614, 2002.

- [14] F. E. Curry and R. H. Adamson, "Endothelial Glycocalyx: Permeability Barrier and Mechanosensor," *Annals of Biomedical Engineering*, vol. 40, no. 4, pp. 828-839, 2012.
- [15] H. Luczak and W. Laurig, "An Analysis of Heart Rate Variability," *Ergonomics*, vol. 16, no. 1, pp. 85-97, 1973.
- [16] P. Vincent, "A Cellular Scale Study of Low Density Lipoprotein Concentration Polarisation in Arteries," Department of Aeronautics, Imperial College London, London, 2009.
- [17] V. Peiffer, E. M. Rowland, S. G. Cremers, P. D. Weinberg and S. J. Sherwin, "Effect of aortic taper on patterns of blood flow and wall shear stress in rabbits: Association with age," *Atherosclerosis*, vol. 223, no. 1, pp. 114-121, 2012.